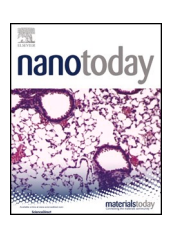


Contents lists available at ScienceDirect

Nano Today

journal homepage: www.elsevier.com/locate/nanotoday



Na⁺ inserted metal-organic framework for rapid therapy of bacteriainfected osteomyelitis through microwave strengthened Fenton reaction and thermal effects



Shubin Wei^a, Yuqian Qiao^b, Zhengchen Wu^c, Xiangmei Liu^{a,*}, Yuan Li^b, Zhenduo Cui^b, Changyi Li^d, Yufeng Zheng^e, Yanqin Liang^b, Zhaoyang Li^b, Shengli Zhu^b, Hairen Wang^a, Xianbao Wang^a, Renchao Che^{c,*}, Shuilin Wu^{b,*}

- ^a Hubei Key Laboratory of Polymer Materials, School of Materials Science & Engineering, Hubei University, Ministry-of-Education Key Laboratory for the Green Preparation and Application of Functional Materials, Wuhan 430062, China
- ^b School of Materials Science & Engineering, The Key Laboratory of Advanced Ceramics and Machining Technology by the Ministry of Education of China, Tianjin University, Tianjin 300072, China
- ^cLaboratory of Advanced Materials, Department of Materials Science and Collaborative Innovation Center of Chemistry for Energy Materials (iChem), Fudan University, Shanghai 200438, China
- ^d Stomatological Hospital, Tianjin Medical University, Tianjin 300070, China
- ^e College of Engineering, State Key Laboratory for Turbulence and Complex System, Department of Materials Science and Engineering, Peking University, Beijing 100871, China

ARTICLE INFO

Article history: Received 4 December 2020 Received in revised form 5 January 2021 Accepted 21 January 2021

Keywords:
Antibacterial
Osteomyelitis
Prussian blue
Microwave
Fenton reaction

ABSTRACT

The poor penetration ability of light in tissues makes phototherapy be difficult to treat bacteria-induced osteomyelitis effectively. Herein, we developed a rapid and noninvasive therapeutic strategy by employing Prussian blue (PB) as a microwave-responsive material. The PB was excited by microwave through dielectric loss of PB and the changed spin state of iron ions, which led to the heat generation and then weakened the bond energy of Fe II–(CN) and Fe III–(NC) in physiological saline. At the same time, the insertion of Na⁺ in PB made the bond energy become irreversible, which accelerated the release of Fe²⁺ and Fe³⁺ from PB. The released Fe²⁺ and Fe³⁺ could be easy to penetrate bacterial membrane with reduced permeability by microwave to react with H_2O_2 and GSH in the inside of bacteria, leading to the final death of the bacteria due to the synergistic action of microwave, microwave thermal effect and Fe²⁺/Fe³⁺ induced Fenton reaction/GSH consumption. This study will provide novel insight for designing remote and noninvasive antibacterial systems for treating deep bacteria-infected diseases.

© 2021 Published by Elsevier Ltd.

Introduction

Since the discovery of Penicillin by Fleming, various antibiotics have been developed to treat bacteria-induced diseases including osteomyelitis [1]. However, long treatment time and excessive use of antibiotics have been inducing bacterial resistance and emergence of superbugs, which make antibiotics ineffective [2–4]. Traditional inorganic antibacterial materials, such as Ag-based antibacterial agents and metal oxides (ZnO, CuO and etc.), not only exhibit some tissue toxicity and but also need more time to kill bacteria [5–8]. The

E-mail addresses: liuxiangmei1978@163.com (X. Liu), rcche@fudan.edu.cn (R. Che), shuilinwu@tju.edu.cn, shuilin.wu@gmail.com (S. Wu).

recent studies disclosed that the phototherapy is effective for bacteria-killing in a short time and can avoid bacterial resistance [9–11]. However, bacteria-induced osteomyelitis occurs in deep bone tissue, where lights even near infrared (NIR) light cannot arrive. Microwave (MW) with strong penetration ability may be an ideal substitute of light for treatment of deep tissue infection [12].

However, the higher temperature and long treatment time, that are required for effective inactivation of bacteria, can scald normal tissues inevitably, it is difficult to utilize microwave to treat bacterial infections directly [13]. Hence, it is necessary to develop biocompatible materials with much stronger microwave-absorbing ability than surrounding tissues [14,15]. At present, materials capable of absorbing MW are mainly divided into three kinds of categories including magnetic loss materials, dielectric loss materials, and materials with multiple voids [16]. Metal-organic framework

^{*} Corresponding authors.

(MOF) as one kind of mesoporous materials can achieve multiple reflection and refraction of MW. As a typical mesoporous MOF, Prussian blue (PB) is expected to become an efficient MW heat conversion material. In addition, PB has been approved for clinical application by the US Food and Drug Administration and contains a large amount of Fe(II) and Fe(III) [17,18]. The large amount of iron ions can achieve Fenton reaction by react with $\rm H_2O_2$ in bacteria, thus producing hydroxyl radical (•OH) with very strong oxidation ability [19]. In addition, most of the iron ions in bacteria can be bound to proteins in the bacterial environment [20]. It has been reported that bacteria have a unique system to strictly regulate the absorption of iron ions by the proteins on the cell membrane [21].

In this work, we developed a Na⁺ inserted PB system, which was employed as the MW-absorbing material and the carrier of iron ions to treat bacteria-infected osteomyelitis. Briefly, PB can absorb MW to generate heat through dielectric loss and reflection of mesoporous structure. At the same time, MW can change spin state of iron ion and their release behavior. The spin state of iron ions is reversible, but the insertion of sodium ions (Na⁺) in the solution can induce the spin state of iron ions to be irreversible. MW irradiation can change the permeability of membrane to allow iron ions to enter the inside of bacteria. Meanwhile, MW can promote Fenton reaction and Glutathione (GSH) consumption in bacteria, which leads to the final death of bacteria. This process can be schematically illustrated in Scheme 1. The *in vivo* tests show that this MW-excited system is highly effective for the treatment of bacteria-infected osteomyelitis within a short time.

Experimental section

Materials

PVP (4.5 g) and $K_3[Fe\ (CN)_6]$ (340.05 mg) were mixed in 60 mL of HCl (0.01 M) and continuously stirred for 30 min to obtain a clear solution, and then the solution was placed in a muffle furnace at 80 °C for 20 h. After that, the synthesized materials were collected after centrifugation, which was subsequently washed 5 times with deionized (DI) water and alcohol successively. Finally, the as-synthesized materials were dried in an oven at 80 °C for 12 h.

Characterization

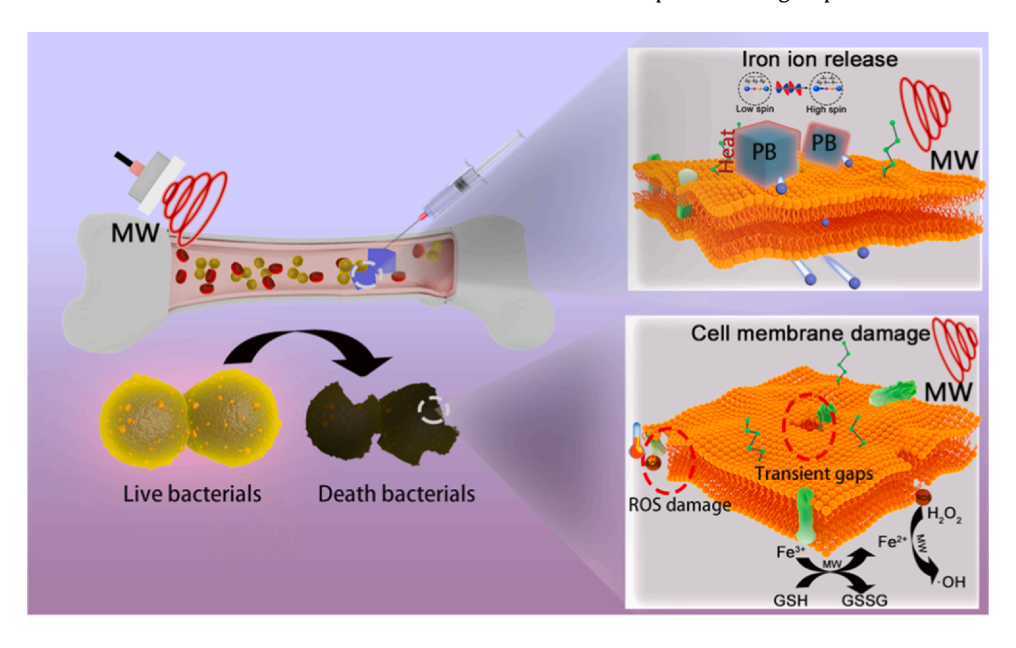
Transmission electron microscopy (TEM, Jem-2100f, Japan) was used to observe the shape and size of the synthesized PB, and their phase structure was characterized by X-ray diffraction (XRD, D8A25, Bruker, Germany). X-ray photoelectron spectroscopy (XPS, Thermo Fisher Scientific 250Xi) was utilized to analyze the valence state of elements. The nitrogen adsorption and desorption behaviors of PB were determined by Brunauer–Emmett–Teller (BET) (JW-BK112).

Measuring microwave heat

The 1 mg mL $^{-1}$ PB was placed in a 2 mL centrifuge tube and the tube was placed on a MW physiotherapy probe. Using a thermal imager (875i, Testo, GER) to record the temperature variation of PB solutions with different concentration (0, 0.5, 1 mg mL $^{-1}$) under 10 W MW irradiation. A thermal imager was utilized to record the temperature of 1 mg mL $^{-1}$ PB solution under the irradiation of MW with different power.

Antibacterial experiment

As the representative of Gram-negative and Gram-positive bacterium, both Escherichia coli (E. coli) and Staphylococcus aureus (S. aureus) were used in antibacterial tests. The bacteria were collected by a refrigerated centrifuge (6000 rpm, 5 min) after discarding the LB medium, and then washed twice with physiological saline. The concentration of bacterial solution was adjusted to 1.0×10^7 CFU mL⁻¹ before antibacterial tests, and 800 µL bacterial solution and $200\,\mu L\ PB\ (5\ mg\ mL^{-1})$ solution were added into a $2\,mL$ centrifuge tube, which was labeled as PB group. The 800 µL bacteria solution and 200 µL physiological saline were used as the control group. The centrifuge tube was placed in a 55 °C water bath for 20 min as the water-bath (55 °C) group. The centrifuge tube was placed in an ice bath under MW irradiation (8 W 5 min, 3 W 15 min) as the PB + MW (17 °C). For comparison, the centrifuge tube directly irradiated by MW (8 W 5 min, 3 W 15 min) without ice bath was used as the PB + MW (55 °C) group. The centrifuge tube was placed on the 0.8 cm pork and then irradiated by MW (8 W 5 min, 3 W 15 min), which was used as the penetration group. The different bacterial liquids were



Scheme 1. Schematic diagram of PB with microwave response for osteomyelitis treatment. PB responds to microwave through dielectric loss and spin crossover structure in physiological saline. At the same time, Iron ions will be released from PB and the insertion of Na⁺ will make the spin-crossing structure irreversible. The released iron ions will synergize with microwave heat to treat bacteria-induced osteomyelitis in rabbits.

taken and diluted 100 times, and then $20\,\mu L$ solution was used for plate coating. The plate was placed in an incubator at 37 °C for 24 h. Antibacterial ratio can be calculated according to the following formula:

Antibacterial ratio(%) =
$$\frac{N_{control} - N_{sample}}{N_{control}} \times 100\%$$

Here $N_{control}$ is the number of bacterial colonies in the control group while the N_{sample} is the number of bacterial colonies in the experimental group. The morphology of the bacteria was observed by FESEM (Zeiss sigma 500, Germany). The treated bacterial solution was removed from the LB medium, and then the bacteria were fixed by adding 2.5 glutaraldehyde solution for 2 h and subsequently dehydrated using 30%, 50%, 70%, 90% and 100% alcohol successively for 15 min. Finally, these samples were examined by FESEM after drying. In order to detect the change of element content inside bacteria, TEM and EDS were utilized to detect the microstructure and internal element content of bacteria, respectively. Briefly, the bacteria were collected through a refrigerated centrifuge (6000 rpm, 5 min) by discarding the supernatant. Then 2.5% glutaraldehyde and 1% OsO4 aqueous osmium were added to fix the collected bacteria by mixing for 2 h. The fixed bacteria were washed three times with PBS, and then dehydrated with different gradients of alcohol (30%, 50%, 70%, 90%, 100%) successively for 15 min. Finally, the bacteria were embedded in resin and sliced (Google Biological, Wuhan) for further TEM examination.

ROS determination of material

The method of degrading Rhodamine B (RhB) by ROS was adopted to evaluate the level of ROS produced by MW-irradiated materials. $200\,\mu L$ PB $(5\,mg\,mL^{-1})$ was added to $800\,\mu L$ RhB $(10\,mg\,L^{-1})$ with continuous stirring for 30 min in the dark, and then the mixed solution was subjected to MW irradiation. The absorption values at $500\text{--}600\,nm$ were measured by microplate reader (SpectraMax I3, Molecular Devices).

Fenton reaction test

In order to investigate the effect of PB on oxidative stress inside bacteria, we added GSH as an antioxidant in bacteria, and Fe(III) was reduced to Fe(II) by GSH. Briefly, 1×10^{-3} M GSH was added into PB solution (1 mg mL⁻¹), and then RhB (1×10^{-6} M) and H₂O₂ (1×10^{-6} M) were added into the above mixed solution after the material and GSH adsorption/desorption for 2 h. Finally, the absorption of the solution was measured by a microplate reader at a wavelength of 500-600 nm.

ROS detection inside bacteria

The level of ROS inside bacteria was measured by 2′,7′-Dichlorodihydrofluorescein diacetate (DCFH-DA), The bacteria were collected by a refrigerated centrifuge (6000 rpm, 5 min) after discarding the LB medium, and then washed twice with physiological saline. After that, DCFH-DA (0.5 $\mu L\,mL^{-1}$) was added into the above collected bacteria and co-cultured in an incubator for 30 min at 37 °C. The co-cultured DCFH-DA was removed by using a refrigerated centrifuge (6000 rpm, 5 min). The above bacterial solution was diluted with physiological saline to an OD600 of 0.05–0.1, and finally, after MW irradiation, the relative fluorescence intensity was measured by a microplate reader (excitation at 488 nm and emission at 525 nm).

Bacterial inner membrane permeability test

o-nitrophenyl- β -D-galactoside (ONPG) was used to assess the intimal permeability of *S. aureus*, isopropyl- β -D-thiogalactoside (IPTG) was co-cultured with the bacteria for 12 h and the LB medium was discarded by a centrifuge (6000 rpm, 5 min). The obtained bacteria were washed twice with physiological saline and then diluted to an OD₆₀₀ value of 0.05–0.1. 1 mg mL⁻¹ PB solution was added into the diluted bacterial solution under MW irradiation. Finally, 15 μ L treated bacterial solutions,15 μ L ONPG (12.5 mM),10 μ L dimethyl sulfoxide,110 μ L physiological saline were mixed together, and then the absorption of the solution in the OD₄₂₀ were recorded by a microplate reader.

Bacterial outer membrane permeability test

The evaluation of outer membrane permeability of *E. coli* was carried out by using ANS (8-anilinonaphthalene-1-sulfonic acid). The LB medium in the bacterial solution was discarded by using a refrigerated centrifuge. After adding physiological saline, the supernatant was discarded by a refrigerated centrifuge, and this process was repeated twice. The cleaned bacterial solution was added to ANS (0.316 mg L⁻¹) and co-cultured in an incubator for 20 min at 37 °C. The relative intensity of fluorescence was measured with a microplate reader after MW irradiation (excitation at 380 nm and emission at 460 nm).

Release of iron ions

The PB solution was placed in a 2 mL centrifuge tube and subjected to MW irradiation for 20 min, and then centrifuged at 10,000 rpm for 20 min to obtain a supernatant. The concentration of iron ions in the solution can be quantitatively determined by an inductively coupled plasma-atomic emission spectrometry (ICP-AES).

Material toxicity test

The mesenchymal stem cells (MSCs) (The third generation MSCs from Tongji hospital in Wuhan, China.) were chosen as the experimental cells to assess the cytotoxicity of the materials. Briefly, osteoblasts and PB (1 mg mL $^{-1}$) solution were added to the culture dish and incubated in an incubator of 5% CO $_2$ at 37 °C for 24 h. After that, the culture medium was discarded, and the MTT solution (0.5 mg mL $^{-1}$, 800 μ L) was added into the dish with the followed incubation for 4 h under the aforementioned condition. Next, the MTT solution was discarded, and 800 μ L of dimethyl sulfoxide was added with continuous shaking for 15 min. The absorbance of the solution at OD at 490 or 570 nm was measured using a microplate reader. The cell viability can be calculated according to the following formula:

Cell viability(%) =
$$\frac{OD_{sample}}{OD_{control}} \times 100\%$$

Inflammatory response

In order to evaluate the effects of *S. aureus* on inflammatory response, the lipopolysaccharide (LPS) of *S. aureus* membrane was extracted and mixed with macrophage and PB. Briefly, the experiment was divided into three groups: RAW264.7 cells group, RAW264.7 cells + LPS, RAW264.7 cells + LPS + PB. RAW264.7 cells (obtained from Tongji hospital in Wuhan, China) were used in this experiment. After the cells were cultured in an incubator of 5% CO₂ at 37 °C for 12 h, DCFH-DA was added and incubated for 1 h

subsequently. Next, this DCFH-DA containing medium was discarded, and the culture dish was washed with PBS. PBS and PB containing LPS solutions were added and placed in an incubator of 5% CO₂ at 37 °C for 5 h. After that, the well was washed with PBS after discarding the liquid in the well, and then the fluorescence image was observed by an inverted fluorescence microscope (IFM, Olympus, IX73).

In vivo antibacterial assay

Rabbits (2.5-2.9 kg body weight) were obtained from Keda Breeding Center (Tianjin, China). A total of 18 rabbits were placed in cages, and each cage contains two rabbits. These rabbits were randomly divided into three groups (Control, PB and PB+MW). After anesthetizing the rabbits with anesthesia, a hole of 0.6 mm diameter was drilled in the tibia using an electric drill. 250 mL of blood in the bone marrow cavity was drawn out with a 2.5 mL syringe, and 100 mL of bacterial solution (2.0 \times 10⁶ CFU mL⁻¹ S. aureus) with 100 mL physiological saline solution or 100 mL PB (1 mg mL⁻¹) was injected into the hole. Afterwards, the hole was sealed with bone wax. The wound was then sutured and irradiated with a MW physiotherapy instrument for 20 min. The thermal imaging pictures were recorded before and after irradiation by using a thermal imager (FLIR, E50). After 0, 2, and 4 days feeding, the blood was collected from each rabbit for routine blood tests and the bone marrows were taken for H&E and Giemsa staining. The main organs of the rabbit (heart, liver, spleen, lung, kidney) were taken for H&E staining at 2 and 4 days. This work was conducted under the guidance of Guide for the Care and Use of Laboratory Animals of the National Institutes of Health. The Animal Ethical and Welfare Committee (AEWC) of the Institute of Radiation Medicine, Chinese Academy of Medical Sciences approved the ethical part of the experiment.

Electromagnetic parameter measurement

The as-prepared sample was uniformly mixed with the melted paraffin by a mass ratio of 3:1 and then modeled into a coaxial hollow pipe with the inner and outer diameters of 3.04 and 7.00 mm, respectively. The electromagnetic parameter within 10 MHz to 18 GHz of the shaped composite was recorded on a HP8510C vector parameter network. The reflection loss value was calculated as follows:

$$RL = 20 \left| \frac{Z_{in} - 1}{Z_{in} + 1} \right|$$

$$Z_{in} = \sqrt{\frac{\mu_r}{\varepsilon_r}} \tanh \left\{ j(\frac{2\pi f d}{c}) \sqrt{\mu_r \varepsilon_r} \right\}$$

where RL represents reflection loss coefficient, $Z_{\rm in}$ refers to the normalized input impedance, μ_r and ε_r are the relative permeability and permittivity, respectively, f is frequency, c is the velocity of light, and d is the thickness of single layer absorber.

Statistical analysis

All the data in those experiments were performed as mean with standard $n \ge 3 \pm SD$. Data were compared via one-way ANOVA or two-way ANOVA and the *p < 0.05 is statistically significant.

Results and discussion

Synthesis and characterization of PB

As shown in Figs. 1a and S1, both the transmission electron microscope (TEM) and scanning electron microscope (SEM) disclosed

that the synthesized PB exhibited nanocubic structure. The high resolution TEM (HRTEM) image showed the spacing lattice of 0.241 nm, 0.498 nm and 0.342 nm (Fig. 1b–e), corresponding to the crystal plane of (400), (200) and (220), respectively, suggesting the successful synthesize of PB nanocubes. After MW radiation, the PB still maintains its original nanocubic-like structure (Fig. 1f). However, the HRTEM image (Fig. 1g–j) displayed that the lattice gap of PB increases slightly. The energy disperses spectroscopy (EDS) obtained from MW-irradiated PB immersed in physiological saline shows the existence of C, N, O, Fe and Na elements (Fig. S2). Base on the above data, it cloud be drawn that the Na⁺ was inserted into the structure of PB under MW irradiation, resulting in the spacing lattice change of PB [22], which was schematically illustrated in Fig. 1k.

We further analyzed the changes of the PB structure after MW irradiation through XRD. We magnified the (200), (220) and (400) peaks in Fig. S3 for further observation. Obviously, the peaks of (200), (220) and (400) show different degrees of shift to lower degree (Fig. 2a-c), which was in good agreement with the results of HRTEM shown in Fig. 1. In order to further explore the changes of PB microstructure after MW, X-ray photoelectron spectroscopy (XPS) was utilized to determine the fluctuation of binding energy. In the case of Fe 2p XPS spectrum (Fig. 2d and e), the Fe(II) fitting peaks were located at 708.4 and 721.3 eV $(2p_{3/2}$ and $2p_{1/2})$, while Fe(III) fitting peaks were located at 713.2 and 725.8 eV $(2p_{3/2}$ and $2p_{1/2})$ [23]. After MW radiation, the Fe(II) fitting peaks were located at 708.1 and 721.2 eV $(2p_{3/2}$ and $2p_{1/2})$, while Fe(III) fitting peaks were located at 712.9 and 725.7 eV ($2p_{3/2}$ and $2p_{1/2}$). Obviously, the ratio of Fe(II)/Fe(III) was increased from 2.55 to 2.84 after MW irradiation, suggesting that the iron ions were separated in PB structure, and MW irradiation induced the change of the ratio of different valence iron ions in PB, which could be further confirmed by Fig. 2f. The binding energies of Fe III-(NC) and Fe II-(CN) were 713.2 and 708.4 eV (Fig. 2f) [24]. Apparently, the binding energies of Fe III-(NC) and Fe II-(CN) shift to be low energy after MW irradiation, and the trend of Fe II-(CN) was more obvious. It is further proved that MW irradiation led to the decrease of Fe III-(NC) and Fe II-(CN) bonds, resulting in the escape of iron ions from the PB structure by slipping the leash of N and C binding in PB. We further verifies the results of XPS by separately evaluating the iron ion concentration before and after MW irradiation of PB. Fig. 2g showed that the amount of iron ions released in the MW + PB group (about 5-fold), which was consistent with XPS results. The nitrogen adsorption measurement was utilized to prove that the pores of PB could allow Na⁺ to be more easily inserted into the PB structure (Fig. 1h). In this course, PB was examined by a nitrogen adsorption and desorption experiment at 77 K. The surface area of PB obtained by Brunauer-Emmett-Teller (BET) was 15.562 m² g⁻¹, and the pore size distribution of PB@MOF was composed of micropores (27.8 nm). Based on the above data, as a spin crossover structure material, PB was susceptible to electromagnetic field, inducing the change of the status of iron ions in PB from low-spin to high-spin [25]. Microwave can realize this process, the spin state changes and the bond length also become longer [26]. Na⁺ were easier to insert into the structure of PB when the spin state of the iron ion changed and the binding energy weakened gradually. Meanwhile, Na⁺ insertion accelerated the release of iron ion under microwave radiation, resulting in irreversible spin state.

MW thermal effects of PB

Under microwave radiation, it is necessary to selectively heat the target and protect the normal tissues from hyperthermia. The MW mainly transfers energy through electromagnetic fields [27], the MW thermal effects of PB was investigated under the electromagnetic field of MW. As shown in Fig. 3a, the temperature of PB solution increased with the increase of material concentration under MW (10 W) irradiation. For the 1 mg mL⁻¹ PB solution, the temperature

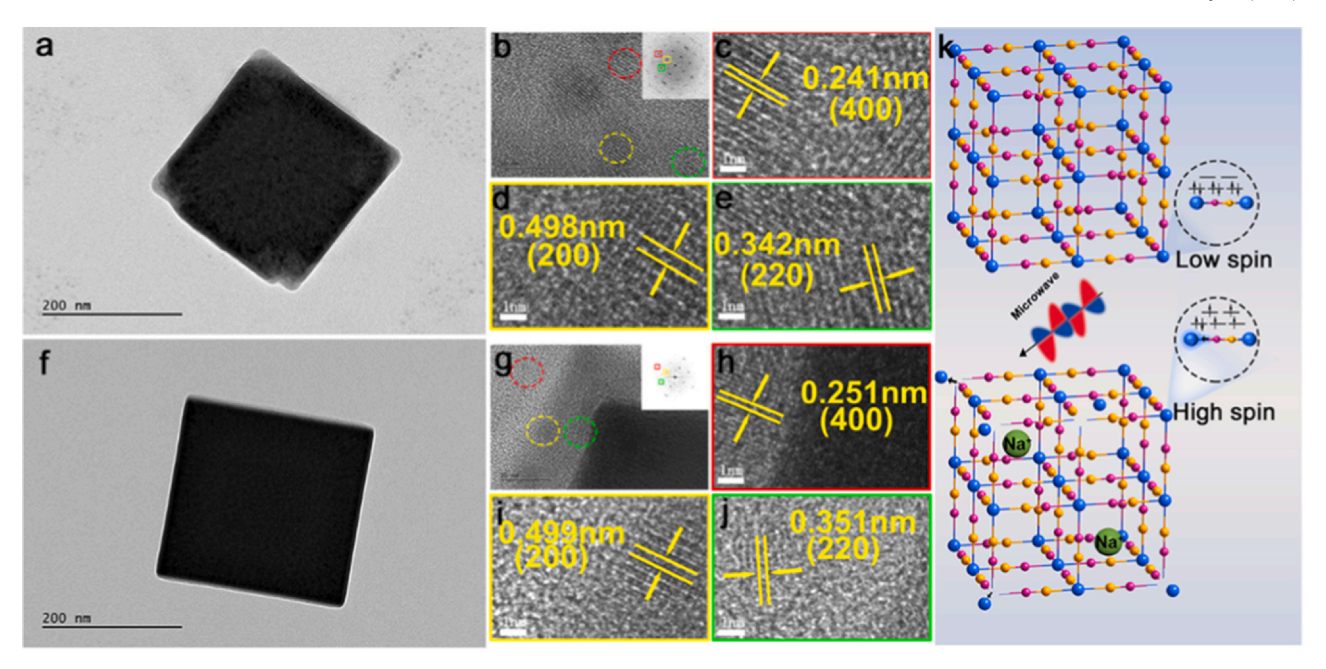


Fig. 1. Morphology and structure characterization of PB and PB-MW. (a) TEM images of PB. (b-e) HRTEM of PB. (f) TEM images of PB-MW. (g-j) HRTEM of PB-MW. (k) Schematic diagram of the structural changes of PB and PB-MW.

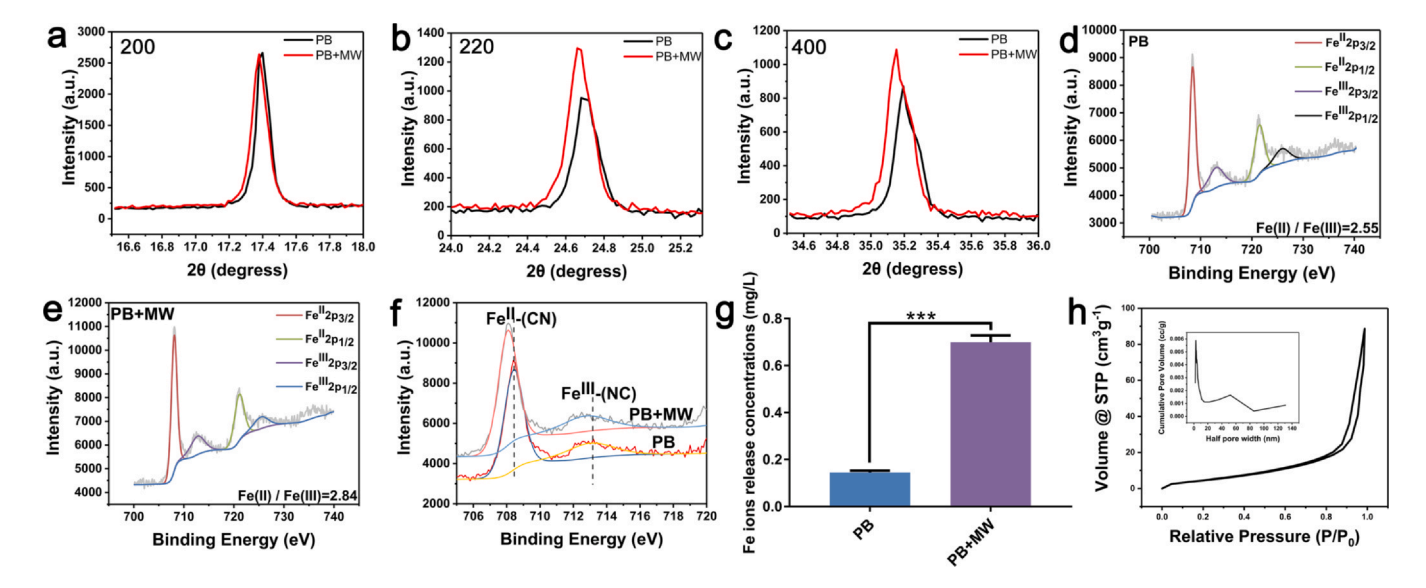


Fig. 2. XRD patterns of PB, magnifications of the (200) peaks (a), the (220) peaks (b) and the (400) peaks (c). XPS spectra of Fe2p of PB (d) and PB-MW (e). (f) XPS spectra of Fe II–(CN) and Fe III–(NC). (g) The amount of iron ions released by PB under microwave irradiation. (h) N₂ adsorption-desorption isotherms at -196 °C and the pore size distribution of PB. (n = 3, *p < 0.05, **p < 0.01, ***p < 0.001, ***p < 0.001).

increased to 65 °C only after 5 min MW irradiation. As a contrast, the physiological saline only rose to 50 °C under the same condition. The results disclosed that PB exhibited excellent MW thermal effects. The influence of MW powers on the MW thermal effects was shown in Fig. 3b. Obviously, the temperature of PB solution increased as the MW power increased, suggesting that there was no obvious threshold in the heating curve of PB when MW power changed. The stability of MW thermal effects of PB was measured by cycle testing. As shown in Fig. 3c, PB solution could still reach 56 °C within 5 min MW irradiation, indicating that PB had excellent MW thermal stability. These results further verified that the structure of PB did not be destroyed by MW irradiation and PB could still provide space for reflecting electromagnetic waves, which was consistent with the TEM results. As shown in Fig. 3d, thermal images showed the MW thermal conversion efficiency of the material with different

concentrations. Obviously, 1 mg mL⁻¹ PB solution showed the highest MW thermal conversion efficiency, which was in good agreement with results shown in Fig. 3a. To evaluate the penetration of MW, a piece of pork (0.8 cm) was added between the probe and the material as illustrated in Fig. 3e. The corresponding pictures of thermal imaging was shown in Fig. 3f. It was evident that MW (8 W) could penetrate 0.8 cm thick pork to heat 1 mg mL⁻¹ PB solution to 54 °C after 5 min irradiation while the surrounding tissues could still maintain a relatively low temperature [28]. The underlying mechanism of MW thermal effects of PB were explored by evaluating the absorbing ability of this material. The complex permittivity and reflection loss (RL) curves were collected (Fig. 3g-k). All the real and imaginary permittivity values of three samples decreased with the increase of frequency. In their imaginary permittivity curves, two polarization peaks appeared around 12 and 15 GHz (Fig. 3g and h),

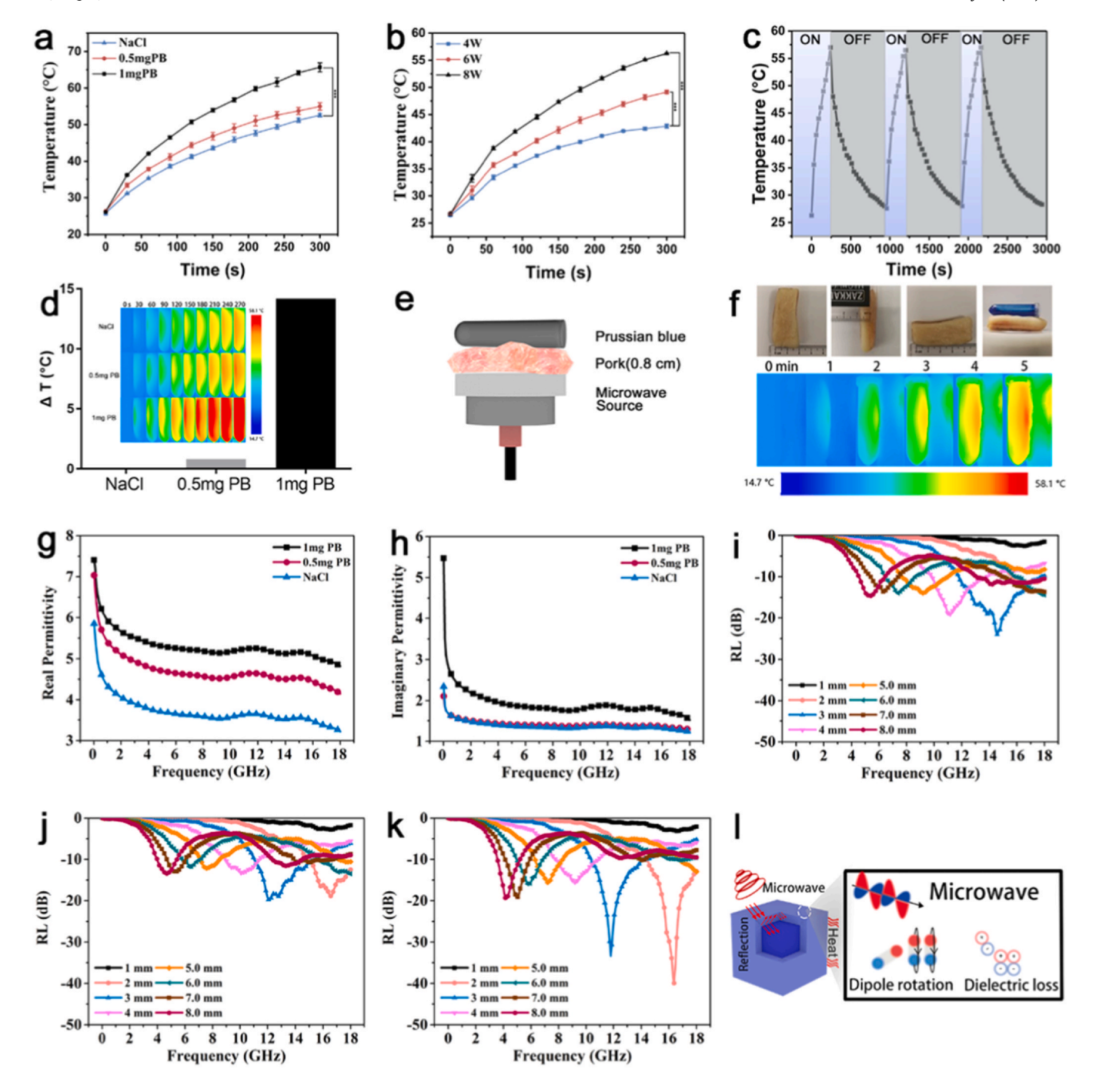


Fig. 3. Characterization of thermal effects and penetration effects. (a) Thermal effects of different concentrations of PB under microwave (10 W) radiation. (b) Thermal effect of PB (1 mg mL $^{-1}$) under different microwave power. (c) PB temperature rise and cooling curve, when the radiation is on/off under microwave. (d) Thermal imaging pictures of different concentrations of PB under microwave (8 W) radiation. (e) Schematic diagram of penetration experiment. (f) Thermal imaging pictures of PB (1 mg mL $^{-1}$) after microwave (8 W) penetration of pork (0.8 cm). The real (g) and imaginary parts (h) of permittivity of all the samples. The reflection loss curves of NaCl (i), 0.5 mg PB (j), and 1 mg PB (k). (l) Schematic diagram of PB generating heat a under microwave. (n = 3, *p < 0.05, **p < 0.01, ***p < 0.001).

respectively. These dielectric relaxation-dominated frequency dispersion features proved that their MW absorption capacities mainly resulted from the dielectric loss properties. The complex permittivity held a positive relationship with the concentration of PB in NaCl solution. Therefore, the 1 mg mL⁻¹ PB with the highest complex permittivity could acquire the strongest dielectric loss capacity as well as the best MW absorption performance. As summarized in Fig. 3i and j, both the pristine NaCl and 0.5 mg mL⁻¹ PB showed RL values less than -20 dB at most frequencies. In comparison, Fig. 3k displayed that the maximum RL values of 1 mg PB could reach -39.9 and -33.4 dB at the thickness of 2 and 3 mm, respectively,

demonstrating its intensified MW dissipation capacity. The process could be schematically illustrated in Fig. 31.

In vitro antibacterial activity

To evaluate the antibacterial performance of PB under MW irradiation, the two types of representative bacteria, *i.e.*, *S. aureus* (Gram-positive bacteria, ATCC 29213) and *E. coli* (Gram-negative bacteria, ATCC 25922) were utilized in this work. As shown in Fig. 4a, the colonies of two types of bacteria on the PB group showed almost the same amount as that on the control group without MW

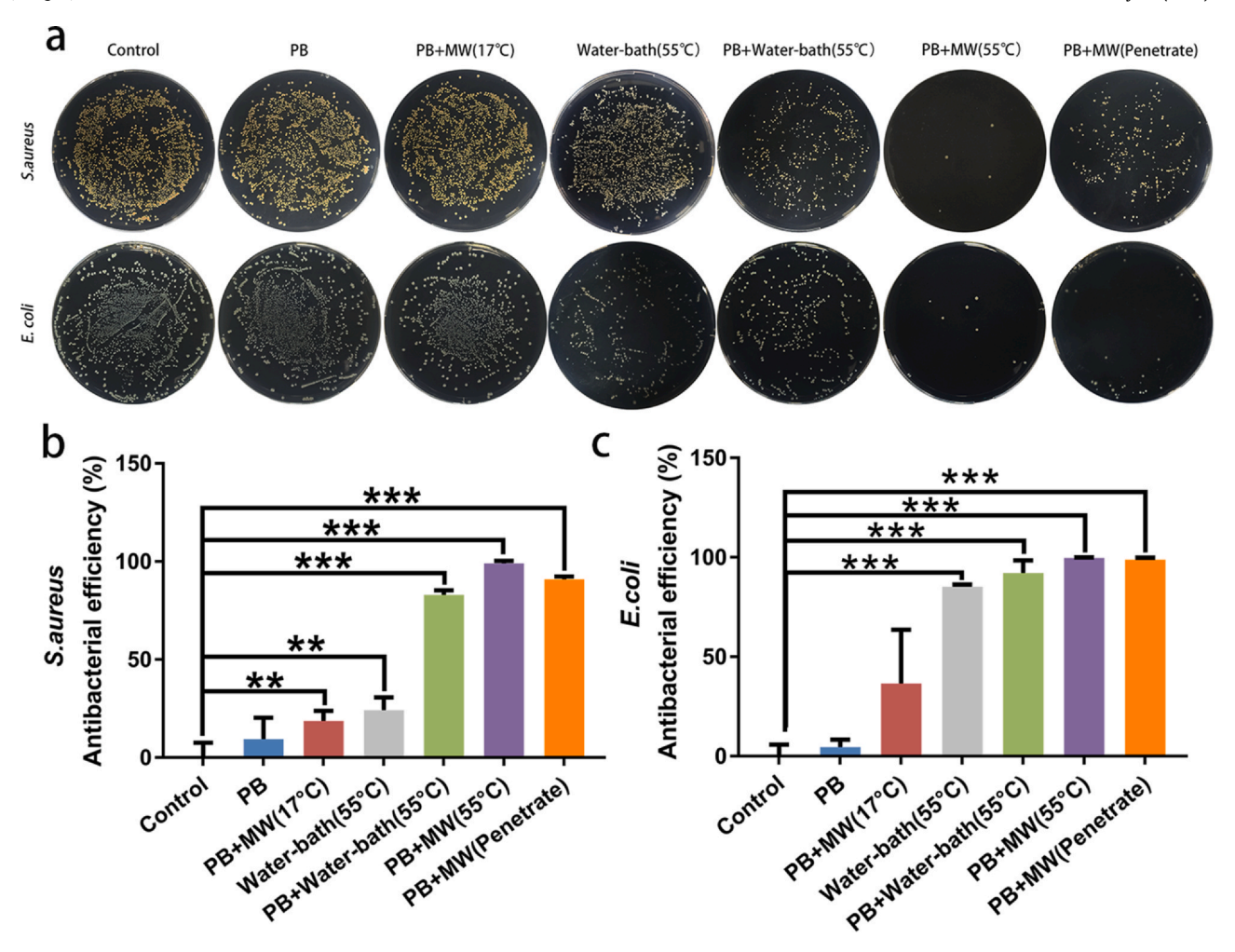


Fig. 4. Antibacterial ability analysis in vitro. (a) Spread plate indicates the growth of viable S. aureus and E. coli colonies after different treatments. Antibacterial rate against S. aureus (b) and E. coli (c) (n = 3, *p < 0.05, **p < 0.01, ***p < 0.001).

irradiation, indicating that pure PB had little antibacterial activity by itself. In order to evaluate the effects of MW and heat separately, the antibacterial efficacy of four kinds of groups (PB + MW(17 °C), waterbath (55 °C), PB + water-bath (55 °C), PB + MW (55 °C)) were measured after treatment for 20 min. Obviously, the bacterial colonies on the group of PB + MW (17 °C) decreased negligibly compared with the one on the groups of PB and the control, suggesting that pure MW irradiation for 20 min without heat had little effect on bacteria. Additionally, the group of PB + water-bath (55 °C) displayed decreased colonies significantly compared with PB and the water-bath (55 °C) groups, which disclosed that the heat intensively enhanced the antibacterial activity of PB. The heat-resistant temperature of gram-positive bacteria is higher than that of gram-negative bacteria, the antibacterial effect of the water bath group on the E. coli is much higher than S. aureus [29]. In contrast, there were almost no bacterial colonies on the group of PB + MW (55 °C). The calculated antibacterial efficiency of the above groups with the order of PB, PB + MW (17 °C), water-bath (55 °C), PB + water-bath (55 °C), and PB + MW (55 °C) was 9.41%, 18.73%, 24.18%, 82.91% and 99.08% against S. aureus (Fig. 4b), and 4.60%, 36.50%, 85.22% 92.07% and 99.67% against E. coli, respectively (Fig. 4c). The above results suggested that only heat, PB, MW + PB or heat + PB could not achieve the best antibacterial efficacy. Only under MW irradiation, PB could achieve the best antibacterial efficiency due to the synergy of MW, MW thermal effects of PB, and PB. Generally, osteomyelitis occurs in the inside of bone tissues, MW has to penetrate the thick soft tissues before reaching the infected sites. The antibacterial activity of PB + MW

(penetrate) group was further investigated by simulating the bacterial infection at depth, *i.e.*, a piece of pig meat with 0.8 cm thickness was added between the centrifuge tube and the physiotherapy instrument probe (Fig. 2e). A high antibacterial efficacy of 97.91% and 98.80% against *S. aureus* (Fig. 4b) and *E. coli* (Fig. 4c) was still achieved after MW irradiation for 20 min with the meat as a barrier, indicating that the energy of MW could be weakened slightly when penetrating tissues.

The morphologies of bacteria from different groups were observed using SEM (Fig. 5a). The bacterial membrane in both the Control and PB groups showed intact profile and no damage occurred. For other groups, the membranes showed various degrees of damage and collapse except for the PB + MW (17 °C) group. Among them, the cell membrane of PB + MW (55 °C) group exhibited the most obvious damage and collapse. These results suggested that damaging bacterial membrane by this system played an important role in bacteria-killing. To further exploring the antibacterial mechanism of MW irradiated PB, TEM was employed to observe the bacterial section and EDS was utilized to detect the elements inside bacteria. As shown in Fig. 5b, compared with the control group, there exist a large amount of blank area in the inside of two kinds of bacteria in the group of PB + MW (55 °C), suggesting that the bacterial membrane was broken and the internal substance of bacteria outflowed. EDS measurement disclosed that iron ions in the both S. aureus and E. coli of the group of PB + MW (55 °C) increased nearly sevenfold compared to that of the corresponding bacteria of the Control group, respectively. These results indicated that iron ions

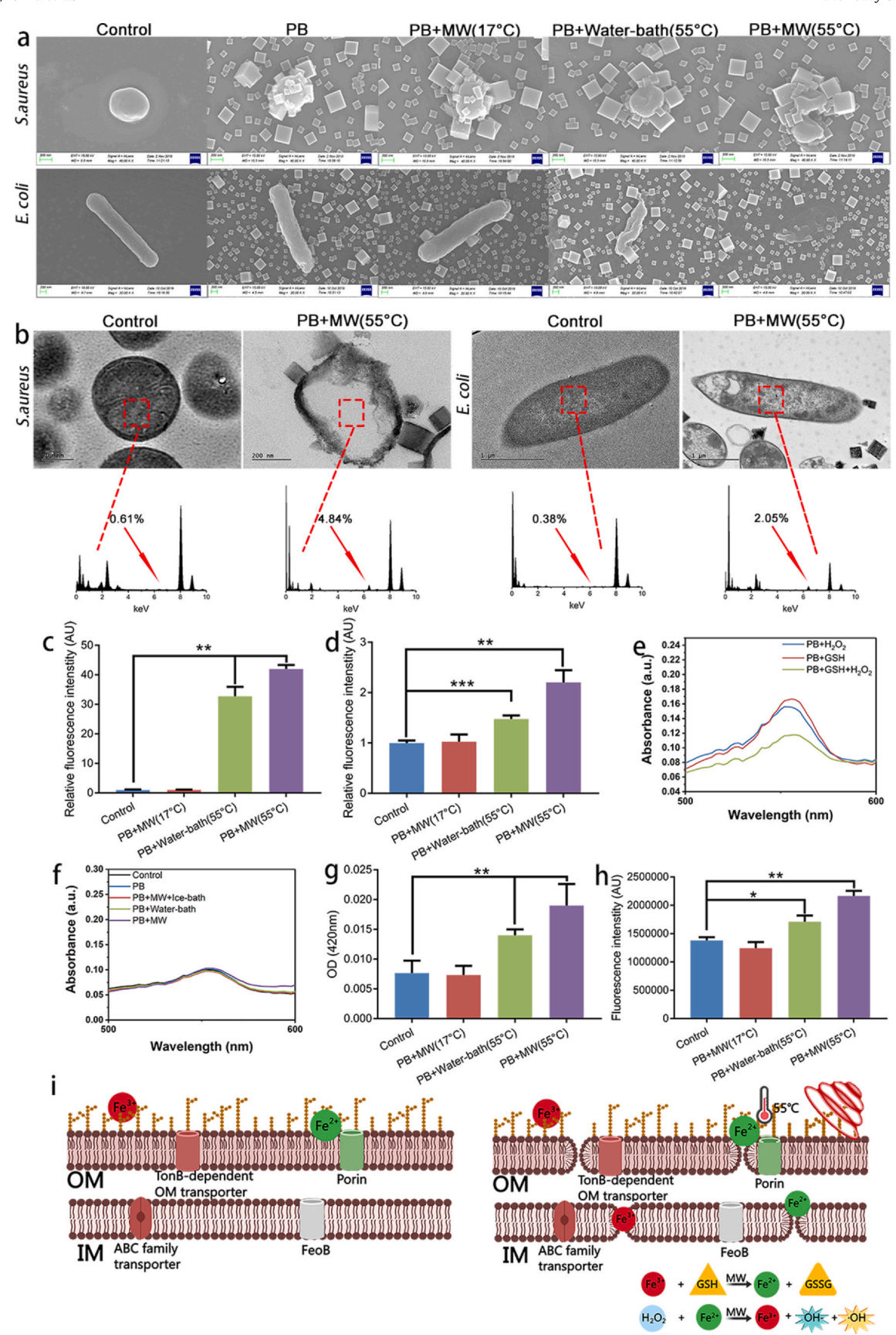


Fig. 5. Antibacterial mechanism. (a) FESEM morphology of *S. aureus* and *E. coli* treated under different conditions. The scale bars were 200 nm. (b) TEM and EDS analysis for *S. aureus* and *E. coli* under different conditions. The scale bars were 200 nm and 1 μm, respectively. ROS in S. aureus (c) and E. coli (d) are generated by PB under different conditions. (e) PB degradation of RHB in different environments under dark conditions. (f) Degradation effect of PB on RHB after treatment under different conditions. (g) The effect of PB on inner membrane permeability of *S. aureus* under different conditions. (h) The effect of PB on outer membrane permeability of *E. coli* under different conditions (n = 3, *p < 0.05, **p < 0.01, ***p < 0.001). (i) Schematic diagram of antibacterial mechanism.

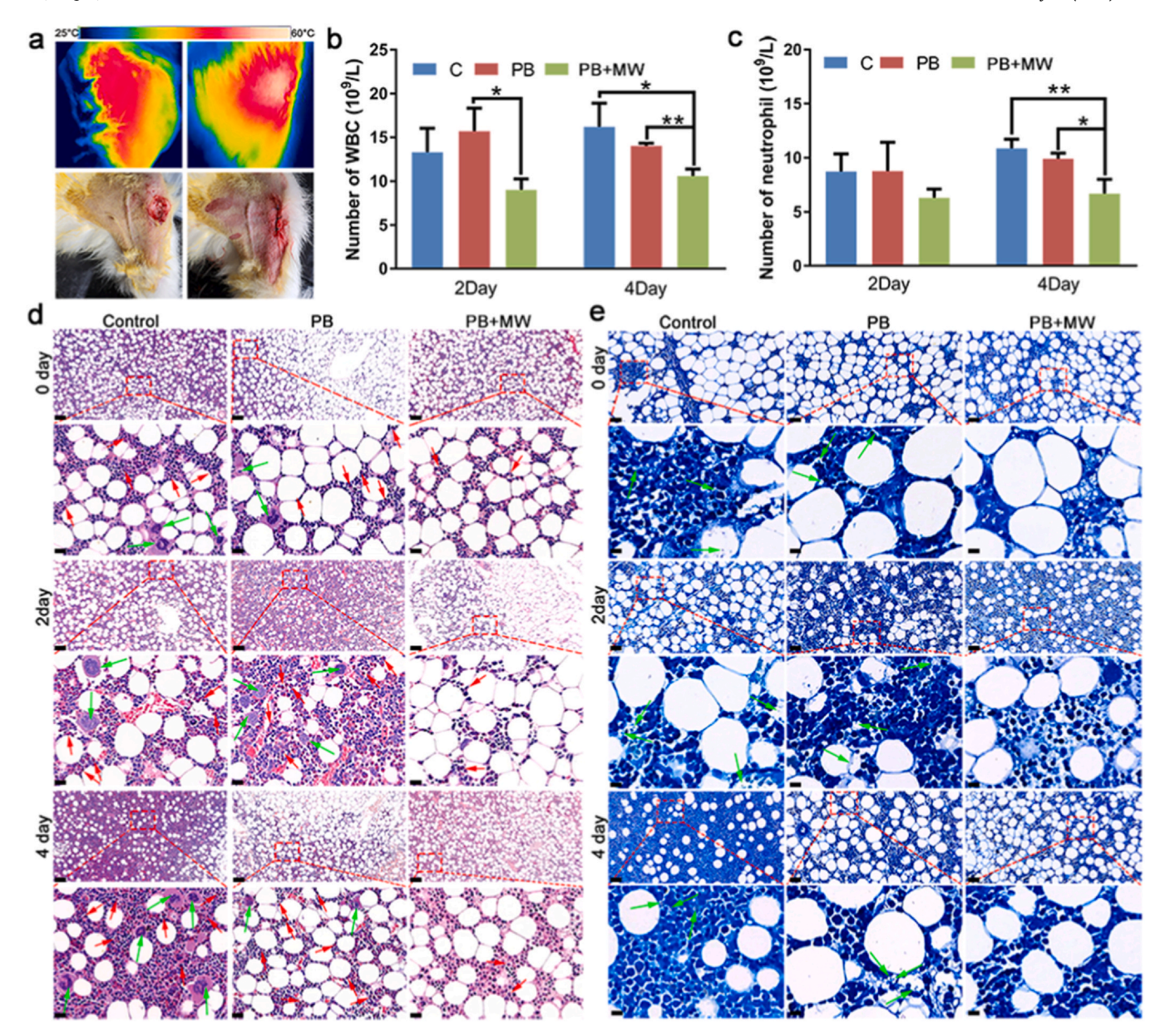


Fig. 6. In vivo antibacterial experiments. (a) Thermal imaging pictures of rabbit bone tissue after microwave radiation. Blood routine examination of the WBC (b) and neutrophils (c). H&E (d) and Giemsa (e) pictures of the Bone marrow tissue after processing separately with Control, PB and MW when the time is 0, 2, 4 days (n = 3, *p < 0.05, **p < 0.01, ***p < 0.001). The scale bars were 100 μ m and 50 μ m, respectively.

entered into the bacteria and participated in the Fenton reaction under MW irradiation. It is noted that the changes of iron ions for *S. aureus* and *E. coli* are quite different (Fig. 5b), which may be ascribed to the different membrane structure of the two kinds of bacteria. It has been reported that bacteria have a unique membrane structure to strictly regulate the absorption of iron ions. In the case of *S. aureus*, the cell membrane used to regulate the absorption of iron ions has only one layer while the cell membrane used to regulate the absorption of iron ions has two layers for *E. coli* [30].

Since iron ions were detected inside the bacteria, and it was speculated that the iron ions could react with the inside metabolic products of bacteria such as H₂O₂ to produce •OH by Fenton reaction. The •OH has strong oxidation ability and can oxidize the inside mass such as proteins and GSH. By using 2',7'-Dichlorodihydrofluorescein diacetate (DCFH-DA), the produced •OH in the inside of bacteria was detected. According to Fig. 5c, ROS yield in the *S. aureus* of the control and PB + MW (17 °C) groups was negligible. In contrast, the amount of ROS in the *S. aureus* produced by PB + MW (55 °C) group

was the largest of 41-fold compared with the one of Control group. The PB + Water-bath (55 °C) group showed 32-fold ROS yield compared to the Control group. In *E. coli*, the trend of ROS production in bacteria was similar to *S. aureus* (Fig. 5d). These results disclosed that the PB + MW (55 °C) group had the most ROS yields in the inside of bacteria produced by Fenton reaction between iron ions and H_2O_2 . H_2O_2 and GSH were further used to simulate the internal environment of bacteria, and then PB, H_2O_2 and GSH were added into the Rhodamine B (RhB) solution, respectively. As shown in Fig. 5e, the degree of RhB degradation indicated the ROS production from the Fenton reaction. With the participation of H_2O_2 and GSH, the largest degradation of RHB was achieved. In contrast, both PB + GSH and PB + H_2O_2 showed much lower degradation of RhB. The result verified that under MW irradiation, the released iron ions from PB reacted with the inside mass of bacteria as following:

$$Fe^{3+} + GSH \rightarrow Fe^{2+} + GSSG \tag{1}$$

$$H_2O_2 + Fe^{2+} \rightarrow Fe^{3+} + OH^- + OH$$
 (2)

In order to investigate if the PB can produce ROS under MW irradiation, RhB was used to detect the ability of PB to generate ROS without the participation of bacteria. As shown in Fig. 5f, no ROS was produced from PB under different conditions without bacteria, verifying that ROS were produced inside bacteria rather than outside. The permeability of S. aureus inner membrane and E. coli outer membrane was evaluated to further investigate the antibacterial mechanism [31,32]. As shown in Fig. 5g, in the case of permeability of S. aureus membrane, both the Control and PB + MW (17 °C) groups showed no significant change. In contrast, with the introduction of heat, the permeability of the inner membranes in PB + water-bath (55 °C) group and PB + MW (55 °C) group changed significantly. It was noted that PB + MW (55 °C) group showed the better inner permeability than PB + water-bath (55 °C) group. Similarly, as shown in Fig. 5h, E. coli outer membrane exhibited the same trend as S. aureus for all groups. The above results could be explained as following. The first point was that heat played an important role in the process of changing the permeability of cell membranes. Another reason was that the electric field of MW could make the cell of membrane destabilization and lead to the formation of transient gaps [33]. Due to the low MW power and pulse frequency MW, it was difficult to achieve better membrane permeability when the temperature is 17 °C. The high permeability of cell membrane under large hyperthermia produced by MW irradiated PB accelerated the entrance of iron ions into the inside of bacteria to achieve Fenton reaction while MW irradiation could also strengthen this course [34,35], resulting in more ROS production. In summary, MW irradiation promoted the release of iron ions from PB, and made the iron ions more easily penetrate bacterial membrane. A large amount of iron ions in bacteria induced more intensive Fenton reaction and oxidation of GSH under MW to produce a large amount of ROS inside the bacteria, resulting in the final death of bacteria by destroying the cell membrane damage and the rapid outflow of substances in the bacteria. This bacteria-killing mechanism was schematically illustrated in Fig. 5i.

In vitro animal experiment

The rabbits were divided into three groups: Control (S. aureus), PB (PB +S. aureus), PB + MW (MW + PB + S. aureus). As shown in Fig. 6a, the osteomyelitis model was established on the tibia of the rabbits. The thermal image showed that the MW group temperature increased from 40 °C to 55 °C after MW irradiation. This phenomenon indicated that the PB in the body still had a good MW thermal effect. The blood routine analysis such as neutrophils and white blood cells (WBC) was utilized to reflect the degree of bacterial infection [36]. The parameters of WBC and neutrophils in the PB + MW group were within the normal range. In contrast, in the Control and PB groups, the white blood cells and neutrophils were much higher than normal, indicating the inflammation reaction in the body (Fig. 6b and c). Hematoxylin and eosin (H&E) and Giemsa staining were used to further assess tibial tissue infection. According to Fig. 6d, for the tissues of the Control and PB groups, a large number of inflammatory cells (green arrows) and neutrophil (red arrows) appeared in the sections. In contrast, as for the PB + MW group, it was found that the entire bone marrow tissue was intact and the inflammatory cells were significantly reduced. Giemsa staining was used to further characterize the bacteria in the tissues (Fig. 6e) [37]. Similarly, the Control and PB group showed visible bacteria (green arrows), while there were almost no bacteria in the PB + MW group. Even after 4 days, there were still no bacteria in the group of PB + MW. The H&E staining of the rabbit's main organs (heart, liver, spleen, lung, kidney) showed that MW treatment did not cause organ trauma and there was no accumulation of nanoparticles in these organs (Figs. S8 and S9).

Conclusion

In this work, we designed a Na⁺ inserted PB microwave responsive system, which exhibited highly effective treatment for deep bacteria-infected osteomyelitis in a short time. Our results disclosed that PB had excellent MW heat conversion ability. At the same time, Na⁺ insertion in PB under MW irradiation could not only accelerate the release of iron ions from PB but also make the iron ion spin state be irreversible. The MW thermal effects combined with its own electric field allowed the iron ions from PB to easily pass through the bacterial membrane to carry out the Fenton reaction and GSH consumption by reacting with H₂O₂ and GSH in the inside of the bacteria, which produce a large amount of ROS in the bacteria. Furthermore, MW accelerated Fenton reaction and GSH consumption in bacteria. The synergy of MW, MW thermal effects and ROS resulted in the final death of bacteria. This work provides a safe, remote, noninvasive and highly effective treatment for deep bacterial infection in a short time.

CRediT authorship contribution statement

Shubin Wei, Xiangmei Liu, Renchao Che and Shuilin Wu: Conceptualization. Shubin Wei, Yuqian Qiao, Zhengchen Wu, Yuan Li, Yanqin Liang, and Zhaoyang Li: Methodology. Renchao Che, Zhenduo Cui, Changyi Li, Yufeng Zheng, Shengli Zhu, Hairen Wang, Xianbao Wang: Data analysis, Resources. Shubin Wei, Yuqian Qiao, Zhengchen Wu: Data curation, Writing-Original draft preparation. Xiangmei Liu, Renchao Che and Shuilin Wu: Writing Review & Editing. Xiangmei Liu, Shuilin Wu: Supervision. Xiangmei Liu: Project administration.

Declaration of Competing Interest

The authors declare that they have no known competing financial interests or personal relationships that could have appeared to influence the work reported in this paper.

Acknowledgments

This work is jointly supported by the National Science Fund for Distinguished Young Scholars (No. 51925104), NSFC (Nos. 51671081, 51871162, and 81870809), and Natural Science Foundation of Hubei Province (No. 2018CFA064), and the National Key Research and Development Program of China (No. 2018YFA0703100).

Appendix A. Supplementary material

Supplementary data associated with this article can be found in the online version at doi:10.1016/j.nantod.2021.101090.

References

- [1] R.I. Aminov, A brief history of the antibiotic era: lessons learned and challenges for the future, Front. Microbiol. 1 (2010) 134.
- [2] Z. Zhao, R. Yan, X. Yi, J. Li, J. Rao, Z. Guo, Y. Yang, W. Li, Y.Q. Li, C. Chen, Bacteria-activated theranostic nanoprobes against methicillin-resistant Staphylococcus aureusinfection, ACS Nano 11 (2017) 4428-4438.
- [3] J. Tian, J. Zhang, J. Yang, L. Du, H. Geng, Y. Cheng, Conjugated polymers act synergistically with antibiotics to combat bacterial drug resistance, ACS Appl. Mater. Interfaces 9 (2017) 18512–18520.
- [4] X. Lv, J. Zhang, D. Yang, J. Shao, W. Wang, Q. Zhang, X. Dong, Recent advances in pH-responsive nanomaterials for anti-infective therapy, J. Mater. Chem. B 8 (2020) 10700–10711.
- [5] J.-M. Zhang, Y.-H. Sun, Y. Zhao, Y.-L. Liu, X.-H. Yao, B. Tang, R.-Q. Hang, Antibacterial ability and cytocompatibility of Cu-incorporated Ni-Ti-O nanopores on NiTi alloy, Rare Met. 38 (2019) 552–560.
- [6] E.-L. Zhang, S. Fu, R.-X. Wang, H.-X. Li, Y. Liu, Z.-Q. Ma, G.-K. Liu, C.-S. Zhu, G.-W. Qin, D.-F. Chen, Role of Cu element in biomedical metal alloy design, Rare Met. 38 (2019) 476–494.

- [7] X. Xie, C. Mao, X. Liu, L. Tan, Z. Cui, X. Yang, S. Zhu, Z. Li, X. Yuan, Y. Zheng, K.W.K. Yeung, P.K. Chu, S. Wu, Tuning the bandgap of photo-sensitive poly-dopamine/Ag3PO4/graphene oxide coating for rapid, noninvasive disinfection of implants, ACS Cent. Sci. 4 (2018) 724–738.
- [8] N. Kashef, Y.Y. Huang, M.R. Hamblin, Advances in antimicrobial photodynamic inactivation at the nanoscale. Nanophotonics 6 (2017) 853–879.
- [9] T. Cui, S. Wu, Y. Sun, J. Ren, X. Qu, Self-propelled active photothermal nanoswimmer for deep-layered elimination of biofilm in vivo, Nano Lett. 20 (2020) 7350–7358.
- [10] C. Cao, W. Ge, J. Yin, D. Yang, W. Wang, X. Song, Y. Hu, J. Yin, X. Dong, Mesoporous silica supported silver-bismuth nanoparticles as photothermal agents for skin infection synergistic antibacterial therapy, Small 16 (2020) 2000436.
- [11] Y. Shi, J. Yin, Q. Peng, X. Lv, Q. Li, D. Yang, X. Song, W. Wang, X. Dong, An acidity-responsive polyoxometalate with inflammatory retention for NIR-II photo-thermal-enhanced chemodynamic antibacterial therapy, Biomater. Sci. 8 (2020) 6093–6099.
- [12] T.Q. Zhang, Z.M. Huang, J.X. Shen, G.Q. Chen, L.J. Shen, F. Ai, Y.K. Gu, W. Yao, Y.Y. Zhang, R.P. Guo, M.S. Chen, J.H. Huang, Ther. Adv. Gastroenterol. 12 (2019) 1756284819862966.
- [13] S. Yu, G. Li, P. Zhao, Q. Cheng, Q. He, D. Ma, W. Xue, Adv. Funct. Mater. 29 (2019).
- [14] X. Zhang, G. Ji, W. Liu, B. Quan, X. Liang, C. Shang, Y. Cheng, Y. Du, Thermal conversion of an Fe3O4@metal-organic framework: a new method for an efficient Fe-Co/nanoporous carbon microwave absorbing material, Nanoscale 7 (2015) 12932–12942.
- [15] M. Green, Z. Liu, P. Xiang, Y. Liu, M. Zhou, X. Tan, F. Huang, L. Liu, X. Chen, Doped, conductive SiO2 nanoparticles for large microwave absorption, Light Sci. Appl. 7 (2018) 87.
- [16] E.J. Lee, J. Bae, K.M. Choi, N.C. Jeong, Exploiting microwave chemistry for activation of metal-organic frameworks, ACS Appl. Mater. Interfaces 11 (2019) 35155–35161.
- [17] W. Zhang, S. Hu, J.J. Yin, W. He, W. Lu, M. Ma, N. Gu, Y. Zhang, Prussian blue nanoparticles as multienzyme mimetics and reactive oxygen species scavengers, J. Am. Chem. Soc. 138 (2016) 5860–5865.
- [18] J. Li, X. Liu, L. Tan, Z. Cui, X. Yang, Y. Liang, Z. Li, S. Zhu, Y. Zheng, K.W.K. Yeung, X. Wang, S. Wu, Zinc-doped Prussian blue enhances photothermal clearance of Staphylococcus aureus and promotes tissue repair in infected wounds, Nat. Commun. 10 (2019) 4490.
- [19] S.C. Andrews, A.K. Robinson, F. Rodríguez-Quiñones, Bacterial iron homeostasis, FEMS Microbiol. Rev. 27 (2003) 215–237.
- [20] M. Rivera, Bacterioferritin: structure, dynamics, and protein-protein interactions at play in iron storage and mobilization, Acc, Chem. Res. 50 (2017) 331–340.
- [21] C.K. Lau, K.D. Krewulak, H.J. Vogel, Bacterial ferrous iron transport: the Feo system, FEMS Microbiol. Rev. 40 (2016) 273–298.
 [22] Q. Yang, F. Mo, Z. Liu, L. Ma, X. Li, D. Fang, S. Chen, S. Zhang, C. Zhi, Activating
- [22] Q. Yang, F. Mo, Z. Liu, L. Ma, X. Li, D. Fang, S. Chen, S. Zhang, C. Zhi, Activating C-coordinated iron of iron hexacyanoferrate for Zn hybrid-ion batteries with 10000-cycle lifespan and superior rate capability, Adv. Mater. 31 (2019) 1901521.
- [23] Y. Luo, J. Li, X. Liu, L. Tan, Z. Cui, X. Feng, X. Yang, Y. Liang, Z. Li, S. Zhu, Y. Zheng, K.W.K. Yeung, C. Yang, X. Wang, S. Wu, Dual metal-organic framework heterointerface, ACS Cent. Sci. 5 (2019) 1591–1601.

- [24] A. Lisowska-Oleksiak, A.P. Nowak, M. Wilamowska, M. Sikora, W. Szczerba, C. Kapusta, Ex situ XANES, XPS and Raman studies of poly(3,4-ethylenedioxythiophene) modified by iron hexacyanoferrate, Synth. Met. 160 (2010) 1234–1240.
- [25] W. Kosaka, K. Nomura, K. Hashimoto, S.-i. Ohkoshi, Observation of an Fe(II) spin-crossover in a cesium iron hexacyanochromate, J. Am. Chem. Soc. 127 (2005) 8590–8591.
- [26] D.A. Reed, D.J. Xiao, M.I. Gonzalez, L.E. Darago, Z.R. Herm, F. Grandjean, J.R. Long, Reversible CO scavenging via adsorbate-dependent spin state transitions in an iron(II)-triazolate metal-organic framework, J. Am. Chem. Soc. 138 (2016) 5594–5602.
- [27] Y. Sun, W. Zhong, Y. Wang, X. Xu, T. Wang, L. Wu, Y. Du, MoS2-based mixed-dimensional van der waals heterostructures: a new platform for excellent and controllable microwave-absorption performance, ACS Appl. Mater. Interfaces 9 (2017) 34243–34255.
- [28] Y. Qiao, X. Liu, B. Li, Y. Han, Y. Zheng, K.W.K. Yeung, C. Li, Z. Cui, Y. Liang, Z. Li, S. Zhu, X. Wang, S. Wu, Treatment of MRSA-infected osteomyelitis using bacterial capturing, magnetically targeted composites with microwave-assisted bacterial killing, Nat. Commun. 11 (2020) 4446.
- [29] M.-C. Wu, A.R. Deokar, J.-H. Liao, P.-Y. Shih, Y.-C. Ling, Graphene-based photothermal agent for rapid and effective killing of bacteria, ACS Nano 7 (2013) 1281–1290.
- [30] M.I. Hood, E.P. Skaar, Nutritional immunity: transition metals at the pathogen-host interface, Nat. Rev. Microbiol. 10 (2012) 525–537.
- [31] C. Mao, Y. Xiang, X. Liu, Y. Zheng, K.W.K. Yeung, Z. Cui, X. Yang, Z. Li, Y. Liang, S. Zhu, S. Wu, Local photothermal/photodynamic synergistic therapy by disrupting bacterial membrane to accelerate reactive oxygen species permeation and protein leakage, ACS Appl. Mater. Interfaces 11 (2019) 17902–17914.
- [32] J. Miao, J. Zhou, G. Liu, F. Chen, Y. Chen, X. Gao, W. Dixon, M. Song, H. Xiao, Y. Cao, Membrane disruption and DNA binding of Staphylococcus aureus cell induced by a novel antimicrobial peptide produced by Lactobacillus paracasei subsp. tolerans FX-6, Food Control 59 (2016) 609–613.
- [33] E.K. Ahortor, D. Malyshev, C.F. Williams, H. Choi, J. Lees, A. Porch, L. Baillie, The biological effect of 2.45 GHz microwaves on the viability and permeability of bacterial and yeast cells, J. Appl. Phys. 127 (2020) 204902.
- [34] F. Kishimoto, M. Matsuhisa, T. Imai, D. Mochizuki, S. Tsubaki, M.M. Maitani, E. Suzuki, Y. Wada, Remote control of electron transfer reaction by microwave irradiation: kinetic demonstration of reduction of bipyridine derivatives on surface of nickel particle, J. Phys. Chem. Lett. 10 (2019) 3390–3394.
- [35] D. Mochizuki, R. Sasaki, M.M. Maitani, M. Okamoto, E. Suzuki, Y. Wada, Catalytic reactions enhanced under microwave-induced local thermal non-equilibrium in a core-shell, carbon-filled zeolite@zeolite, J. Catal. 323 (2015) 1–9.
 [36] C. Mao, Y. Xiang, X. Liu, Z. Cui, X. Yang, K.W.K. Yeung, H. Pan, X. Wang, P.K. Chu,
- [36] C. Mao, Y. Xiang, X. Liu, Z. Cui, X. Yang, K.W.K. Yeung, H. Pan, X. Wang, P.K. Chu, S. Wu, Photo-inspired antibacterial activity and wound healing acceleration by hydrogel embedded with Ag/Ag@AgCl/ZnO nanostructures, ACS Nano 11 (2017) 9010–9021.
- [37] L. Tan, J. Li, X. Liu, Z. Cui, X. Yang, K.W.K. Yeung, H. Pan, Y. Zheng, X. Wang, S. Wu, Small 14 (2018).